WATER RESOURCES RESEARCH, VOL. 49, 1–15, doi:10.1002/wrcr.20109, 2013

A stochastic model for estimating groundwater and contaminant discharges from fractured rock passive flux meter measurements

Özlem Acar,[1,2] Harald Klammler,[1,2,3] Kirk Hatfield,[1,2] Mark A. Newman,[1,2] Michael D. Annable,[2,4] Jaehyun Cho,[2,4] Beth L. Parker,[5] John A. Cherry,[5] Pete Pehme,[5] Patryk Quinn,[5] and Ryan Kroeker[5]

Received 1 August 2012; revised 11 January 2013; accepted 17 January 2013.

[1] Estimation of water and contaminant discharges is an important hydrological problem. Fractured rock aquifers are recognized as highly complex flow and transport systems, and the fractured rock passive flux meter (FRPFM) is a recently tested device to simultaneously measure cumulative water and contaminant mass fluxes in fractures intersecting an observation well (boring). Furthermore, the FRPFM is capable of indicating orientations and directions of flow in hydraulically active ("flowing") fractures. The present work develops a discharge estimator for when FRPFM measurements of fracture fluxes in the direction perpendicular to a transect (control plane) along one or more observation wells are available. In addition, estimation uncertainty in terms of a coefficient of variation is assessed based on a Monte Carlo approach under normalized conditions. Sources of uncertainty considered are spatially random fracture trace locations, random trace lengths, and orientations as well as variability of trace average fluxes (including smooth spatial trends), variability of local fluxes within traces, and flux measurement errors. Knowledge about the trace length distribution, which is commonly not available from borehole surveys, is not required for discharge estimation. However, it does affect the uncertainty assessment, and equations for upper uncertainty bounds are given as an alternative. In agreement with general statistical inference, it is found that discharge uncertainty decreases proportionally with the number of fluxes measured. Results are validated, and an example problem illustrates practical application and performance.

Citation: Acar, Ö., et al. (2013), A stochastic model for estimating groundwater and contaminant discharges from fractured rock passive flux meter measurements, *Water Resour. Res.*, *49*, doi: 10.1002/wrcr.20109.

1. Introduction

[2] Fractured rock formations are complex hydrogeological environments, and predictive means for flow and transport phenomena in this media are severely restricted [*Berkowitz*, 2002]. Particularly, economic and technical challenges are faced for characterization and remediation of dense nonaqueous phase liquid source zones. Today's conventional methods have limited usage in terms of site depiction, monitoring, and simulation of flow and transport processes in fractured rock groundwater systems [*Faybishenko et al*., 2000, 2005; *Dietrich et al*., 2005]. Moreover, quantification of contaminant discharge near source zones is crucial for assessing long-term risk, evaluating remedial performance, and meeting regulatory compliance [*Interstate Technology & Regulatory Council* (*ITRC*), 2010]. The current state of the art technologies are based on using measurements or estimates of Darcy water fluxes (e.g., gradient-conductivity method) and groundwater concentrations (e.g., multilevel sampling) in space and time to estimate contaminant discharges from a source zone. These indirect assessments of contaminant discharges are subject to high (and generally not quantified) uncertainty levels. This is due to the temporal and spatial variability of hydrogeological conditions in inherently heterogeneous fractured rock formations. Some approaches to consistently quantifying mass discharges and uncertainties based on a limited amount of information have been recently presented for porous aquifers [*Li et al*., 2007; *Schwede and Cirpka*, 2010; *Troldborg et al*., 2010; *Beland-Pelletier et al*., 2011; *Cai et al*., 2011] and fractured rock [*Reeves et al*., 2010]. For porous aquifers the use of mass flux measurements (rather than determining water flux and contaminant concentration separately) has already been demonstrated to lead to an enhanced portrayal of contaminated sites [*Feenstra et al*., 1996; *ITRC*, 2010].

[1]Department of Civil and Coastal Engineering, University of Florida, Gainesville, Florida, USA.
[2]Inter-Disciplinary Program in Hydrologic Sciences, University of Florida, Gainesville, Florida, USA.
[3]Department of Environmental Sciences and Sustainable Development, Federal University of Bahia, Barreiras, Bahia, Brazil.
[4]Department of Environmental Engineering Sciences, University of Florida, Gainesville, Florida, USA.
[5]Center for Applied Groundwater Research and School of Engineering, University of Guelph, Guelph, Ontario, Canada.

Corresponding author: H. Klammler, Department of Civil and Coastal Engineering, University of Florida, Gainesville, FL 32611-6580, USA. (haki@gmx.at)

0043-1397/13/10.1002/wrcr.20109

Mass fluxes have been shown to result in improved understanding of plume dynamics and conceptual site models, which are crucial elements for optimization of remediation decisions and actions [*Nichols and Roth*, 2004; *Basu et al*., 2006].

[3] The passive flux meter (PFM) developed by *Hatfield et al*. [2004] and *Annable et al*. [2005] is a direct method for monitoring of time-integrated water and contaminant mass fluxes in porous media over different periods of time (days to months). Spatial interpolation and integration of measured local fluxes over a transect may be used to estimate water and/or contaminant discharges with respective uncertainties [*Klammler et al*., 2012]. Currently, the PFM is the only passive sampler which has proven to effectively measure mass fluxes near source zones [*Verreydt et al*., 2010]. Based on the same principles as the PFM for porous media, the fractured rock passive flux meter (FRPFM) is a technology in development that aims at measuring the magnitudes and directions of cumulative water and contaminant fluxes in fully saturated rock fractures [*Cho et al*., 2011; *Newman et al*., 2009, 2010; *Hatfield*, 2010; *Klammler et al*., 2008]. As seen in Figure 1, the FRPFM is a device composed of an impermeable flexible liner (or packer) and a permeable reactive sorbent layer sandwiched between the impermeable flexible liner and the borehole circumference [*Cho et al*., 2011; *Newman et al*., 2009, 2010; *Hatfield*, 2010; *Klammler et al*., 2008]. The sorbent may be a permeable fabric derived from activated carbon, ion exchange resin, etc. The impermeable flexible liner is typically available in a tube or sock design that is easily fitted into a borehole. Once it is inserted it is inflated (pressurized) with a fluid to cause it to conform to the shape of the borehole so that the permeable sorbent layer is pressed against the borehole wall. Due to the impermeability of the flexible liner, the ambient flow within the fractures does not enter the borehole (thus avoiding major cross-connections between

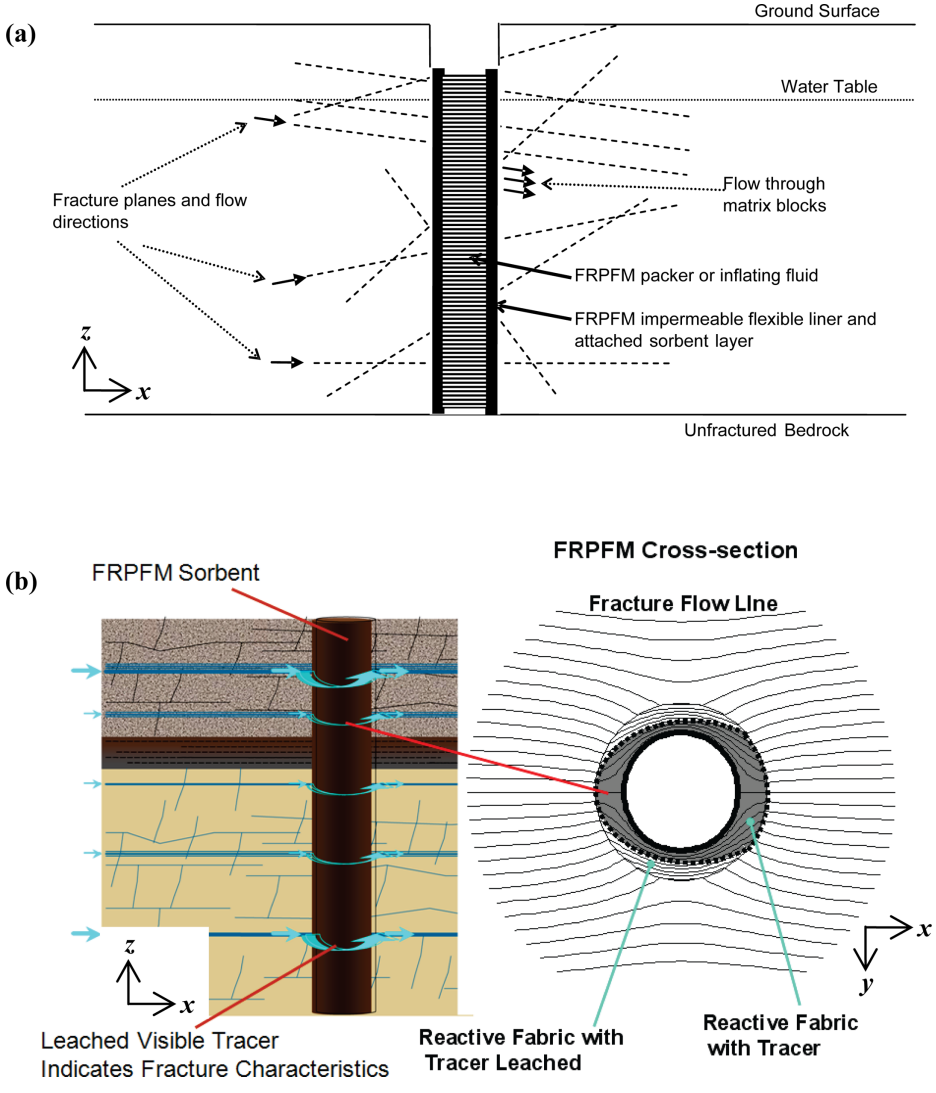

Figure 1. (a) Vertical cross section in the general direction of ambient groundwater flow (*xz* plane) of an unscreened borehole containing a FRPFM. (b) FRPFM installed in (left) a boring and (right) its horizontal cross section. Arrows and flow lines indicate paths of water and advectively driven tracer/contaminant particles.

different fractures and consequently uncontrolled distortion of ambient flow conditions near the borehole). Flow is instead diverted around the impermeable flexible liner (Figure 1b) and passively intercepted by the sorptive layer, which retains target groundwater contaminants (e.g., trichloroethylene (TCE), dichlororethylene (DCE), and vinyl chloride (VC)), while simultaneously releasing nontoxic resident tracers (e.g., visible dyes and/or branch alcohols). The amounts of tracer remaining and contaminant sorbed during a measurement are found from laboratory analysis. Tracer loss is proportional to groundwater flow through the sorbent, and marks of leached visible tracers reveal location and orientation of flowing fractures as well as the direction of flow in the fracture (Figure 1b). Furthermore, contaminant mass captured is proportional to contaminant flux through the sorbent. After correction for flow distortion near the FRPFM [*Klammler*, 2004; *Klammler et al*., 2007], estimates of undisturbed ambient groundwater and contaminant mass fluxes in the fractures are obtained.

[4] In summary, the FRPFM is a potential tool for detecting hydraulically active fractures and determining the following parameters for each of them at the point of intersection with the FRPFM [*Cho et al*., 2011; *Newman et al*., 2009, 2010; *Hatfield*, 2010; *Klammler et al*., 2008]: (1) location or depth; (2) orientation, i.e., strike, dip, and dip orientation; (3) direction of groundwater flow; (4) cumulative (i.e., time-integrated) magnitude of water flux; and (5) cumulative magnitude of contaminant flux. Water and contaminant fluxes are hereby obtained as integral values over fracture aperture (i.e., as fracture discharges per unit fracture length in dimensions of L^2/T for water and M/(LT) for contaminant mass). This eliminates a considerable amount of uncertainty typically introduced by the measurements or estimates of fracture aperture (e.g., for application of cubic law/Hele-Shaw analogue) [*Novakowski et al*., 2006]. In what follows, it is assumed that the FRPFM may reliably provide parameters (1)–(5) for all hydraulically active fractures intersected, where flux magnitudes are associated with a random measurement error. Laboratory and field validation of this capability is conducted as part of an independent research effort. The present work develops a methodology to interpret local flux measurements from FRPFMs in one or more observation wells in terms of water and/or contaminant discharges with associated uncertainties for a transect as shown in Figure 2a, for example. For this purpose, a discharge estimation formula is derived in section 2, and a Monte Carlo simulation is used in section 3 for validation of unbiasedness as well as for developing expressions of estimation uncertainty (e.g., estimation error variance or coefficient of variation (CV)). Section 4 provides validation of results and an example problem for illustration of practical application and performance.

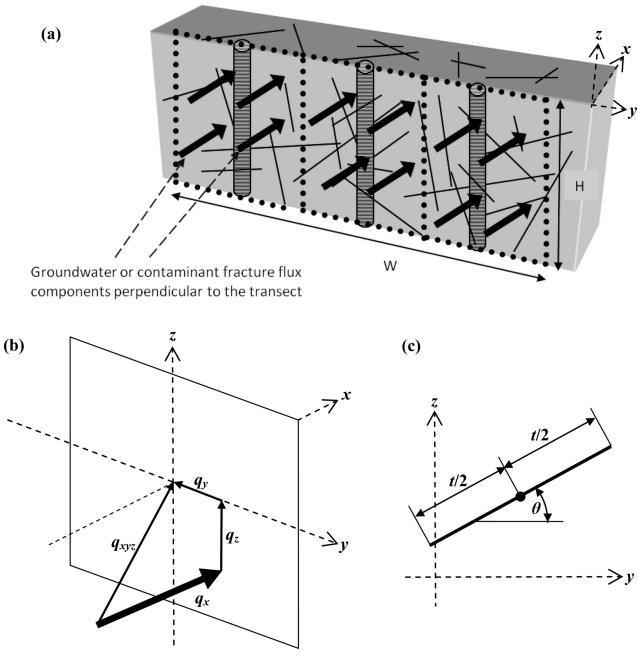

Figure 2. (a) Multiple well transect of width W and height H in fractured rock. Bold arrows represent groundwater or contaminant fracture flux components q_x perpendicular to the transect, which contribute to discharge. (b) Decomposition of 3-D FRPFM measured flux q_{xyz} inside the fracture plane (not shown) into flux vectors q_y and q_z contained in the transect (yz plane) and a vector q_x perpendicular to the transect. (c) Transect plane with a single fracture trace (intersection of fracture plane with transect) of length t and orientation θ taken between $\pm\pi/2$ (dot represents trace midpoint).

2. Development of a Discharge Estimator

2.1. Assumptions

[5] When the flow and transport processes in the fractured media are dominated by fracture zones, it is feasible to describe hydraulic features specifically using a discrete fracture network model [*Helmig*, 1993; *Chiles*, 2005]. Virtually always, the knowledge of in situ individual joint characteristics is limited, which has led discrete network models to be based on stochastic concepts. One of the major drawbacks of discrete fracture network modeling techniques is that some of the detected fractures through conventional borehole measurements can be nonconductive. Since FRPFM measures flow through active fractures only, this concern may be alleviated here. The particular assumptions adopted in the present work for developing a discharge estimator are summarized as follows:

[6] 1. FRPFM only measures advective fluxes through active fractures. Diffusive transport is assumed to be negligible for flow velocities larger than approximately 1 cm/d resulting in Peclet number $Pe > 10$ for characteristic length of 10 cm (approximate FRPFM diameter) and tracer/contaminant diffusion coefficient in water at the order of 1 cm^2/d. Furthermore, advective and diffusive flow through the rock matrix is neglected.

[7] 2. For the present purpose of discharge estimation, only the flux components perpendicular to the transect are considered. These components correspond to q_x in Figure 2b, where the subscript "x" is dropped hereafter for brevity. By definition, flux components inside the transect plane (q_y and q_z in Figure 2b) do not contribute to the discharge.

[8] 3. Fracture traces defined as the intersections of fracture planes with the transect are straight lines of random lengths and orientations (Figures 2c and 3). The statistical properties of trace length and orientation may vary smoothly across the transect.

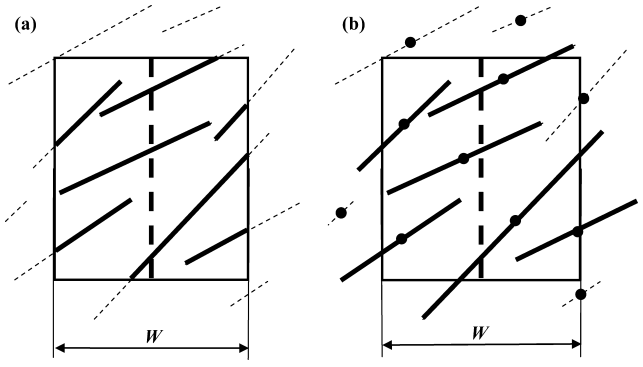

Figure 3. Graphical illustration of (a) true discharge Q and (b) its approximation Q_a. Rectangle represents transect limits containing a single FRPFM (bold dashed). Fracture traces are thin dashed with portions t_i' and t_i contributing to Q and Q_a, respectively, as bold continuous. Dots represent trace midpoints, and heights of both transects are equal to H.

[9] 4. Trace midpoints (center locations of traces as illustrated by dots in Figures 2c and 3b) are assumed to follow a Poisson process, which implies complete randomness of midpoint locations for a given expected number of midpoints per unit transect area (density). Poisson processes are mathematically simple and commonly used in fractured rock hydrogeology [*Chiles and de Marsily*, 1993; *Chiles*, 2005]. The expected density of trace midpoints may vary smoothly across the transect.

[10] 5. The flux variability across a transect consists of three components: (a) a smooth trend function of expected trace average fluxes (e.g., contaminant plume shape); (b) variability of trace average fluxes between traces; and (c) variability of local fluxes within traces.

[11] 6. FRPFMs measure local fluxes within traces at the points of intersection. The observed fluxes are integral values over fracture aperture and include random measurement errors.

[12] 7. The transect may be of arbitrary shape and fully contains one or more parallel (e.g., vertical) FRPFMs of arbitrary lengths.

[13] Note that the analytical development below makes use of basic Poisson properties, but it does not involve any distributional assumptions for trace length, orientation, and fluxes. For illustration in the simulation and example sections, however, uniform, exponential, and log-normal distributions are used as indicated.

2.2. Approximation of True Transect Discharge

[14] In order to develop a discharge estimator, a "true" discharge Q, which is to be estimated, has to be defined. It appears to be a natural choice that Q is taken as the sum of all flows (discharges) through traces or portions thereof, which are contained in the transect as illustrated by the bold portions of traces in Figure 3a. Mathematically, this may be written as

$$Q = \sum_{i=1}^{N'} t_i' q_i, \tag{1}$$

where N' is the number of all traces that are fully or partially contained in the transect, and t_i' are the respective full or partial trace lengths contained in the transect (bold in Figure 3a) conducting average fluxes q_i. Average trace fluxes q_i are hereby considered to be integrated over trace aperture (and projected onto the direction perpendicular to the transect; Figure 2b), such that the product $t_i' q_i$ is the flow through a trace or portion thereof inside the transect; i is an index numerating each trace contributing to discharge. In order to simplify the mathematical development of a discharge estimator, an approximation Q_a to Q will be used in the sequel. As illustrated by Figure 3b, Q_a is defined as the discharge through all traces (of full lengths), whose midpoints are located inside the transect. Hence,

$$Q_a = \sum_{i=1}^{N} t_i q_i, \tag{2}$$

where N is the number of trace midpoints inside the transect, and t_i and q_i are the respective full trace lengths and trace average fluxes (integrated over trace aperture as directly measured by FRPFM and projected onto the direction perpendicular to the transect; Figure 2b). The validity of using Q_a instead of Q will be verified through Monte Carlo simulation later.

2.3. Discharge Estimator for a Single Intersection

[15] At this point, we temporarily limit attention to all traces of orientation θ_j with respect to the horizontal and with average fluxes equal to q_j. The subscript "j" is used to denote all respective variables. A transect discharge Q_{aj} then possesses an expectation μ_{Qaj} (i.e., average over many realizations/ensemble) given by

$$\mu_{Qaj} = q_j \int_{A_T} \lambda_j \mu_{tj} \mathrm{d}A, \tag{3}$$

where dA denotes an infinitesimal portion of the transect area A_T (e.g., of width W and height H as shown for the case of a rectangular transect in Figure 2a), λ_j is the spatially variable Poisson density of midpoints (i.e., the expected number of midpoints per unit transect area), and μ_{tj} is the spatially variable expectation of trace length t. Equation (3) explores the facts that the expectation of trace midpoints inside an infinitesimal transect element dA is equal to $\lambda_j \mathrm{d}A$ and that the expected discharge per trace is equal to $\mu_{tj} q_j$. For constant trace length t_j and orientation θ_j Figure 4a illustrates that the trace midpoints of all traces intersecting a FRPFM of length L_k have to lie within the parallelogram shown, which is of area $L_k t_j \cos\theta_j$. Assuming further that λ_j is spatially constant it is known that the expected number of midpoints in this area (and hence the expected number of intersections) is equal to $\mu_{Njk} = \lambda_j L_k \cos\theta_j t_j$. For t_j following an arbitrary probability distribution with expectation μ_{tj}, the expected number of intersections may be generalized to $\mu_{Njk} = \lambda_j L_k \cos\theta_j \mu_{tj}$. Applying this to an infinitesimal portion dL along L_k for integration and allowing λ_j and μ_{tj} to be variable lead to an expected number of intersections as [*Robertson*, 1970; *Baecher et al.*, 1977; *Long and Witherspoon*, 1985]

$$\mu_{Njk} = \cos\theta_j \int_{L_k} \lambda_j \mu_{tj} \mathrm{d}L, \tag{4}$$

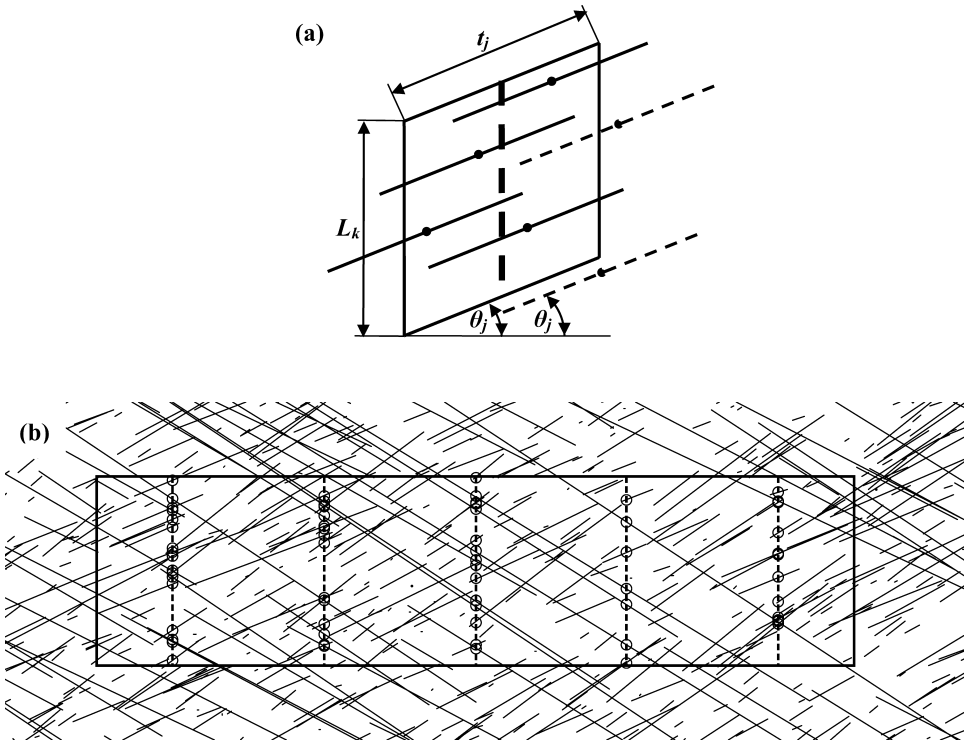

Figure 4. (a) Examples of traces of length t_j and orientation θ_j intersecting (continuous) and not intersecting (dashed) a FRPFM (bold dashed). (b) One stochastic realization of a hypothetical field scenario as used in the example problem and with parameters from Table 1. Transect (bold rectangle; 5 m × 20 m) with five evenly spaced vertical FRPFMs (dashed) intersecting traces (thin continuous) at the circles.

where θ_j is taken between $\pm\pi/2$.Here and in what follows, the subscript $k = 1, 2, \ldots, N_{\text{well}}$ designates one out of N_{well} observation wells across the transect with FRPFM installed.

[16] An unbiased estimator of Q_{aj} for constant q_j and θ_j may be found by substituting unbiased (and uncorrelated) estimators for the unknown terms in equation (3). For this purpose, use is made of the following approximation

$$\frac{1}{A_T}\int_{A_T}\lambda_j\mu_{tj}\mathrm{d}A \approx \sum_{k=1}^{N_{\text{well}}}\frac{\omega_k}{L_k}\int_{L_k}\lambda_j\mu_{tj}\mathrm{d}L = \frac{1}{\cos\theta_j}\sum_{k=1}^{N_{\text{well}}}\frac{\omega_k\mu_{Njk}}{L_k}, \quad (5)$$

where ω_k are weighting constants assigned to each FRPFM, such that $\sum_{k=1}^{N_{\text{well}}}\omega_k = 1$. Equation (5) approximates the areal average of the product $\lambda_j\mu_{tj}$ over the transect by a weighted mean of line averages of $\lambda_j\mu_{tj}$ over all FRPFMs. As a consequence, it appears natural to choose $\omega_k = A_k/A_T$, where A_k is the area, which contains all the points in the transect that are nearest neighbors to the kth FRPFM (this is in analogy to polygonal declustering in classical geostatistics [*Goovaerts*, 1997]). Note that equation (5) becomes exact if $\lambda_j\mu_{tj}$ is constant or if $\lambda_j\mu_{tj}$ only varies in the vertical direction, given that all FRPFMs span the total height of a transect. This is relevant for commonly encountered field situations, where the degree of rock fracturing decreases with depth from the surface. For trends in $\lambda_j\mu_{tj}$ in the horizontal direction, equation (5) represents a stepwise (discrete) approximation, which also becomes exact for equal well spacing in combination with a linear trend function. As such, possible approximation errors of equation (5) may only occur due to higher-order variability in $\lambda_j\mu_{tj}$ in the horizontal direction. The final expression in equation (5) is obtained from eliminating $\int_{L_k}\lambda_j\mu_{tj}\mathrm{d}L$ using equation (4), such that $\int_{A_T}\lambda_j\mu_{tj}\mathrm{d}A$ may be isolated and substituted into equation (3) to express $\mu_{Qaj} = \frac{q_j A_T}{\cos\theta_j}\sum_{k=1}^{N_{\text{well}}}\frac{\omega_k\mu_{Njk}}{L_k}$. According to common statistical practice, the unknown values of μ_{Njk} may be estimated without bias by the samples N_{jk} representing the actual numbers of trace intersections observed on the FRPFMs. Since equation (4) does not discriminate between traces that cause a single or more intersections, μ_{Qaj} also includes the possibility that individual traces may intersect more than a single FRPFM. Yet, without loss of generality, attention may be limited to a single intersection (not a single trace, i.e., $N_{jk} = 1$ for one FRPFM, and $N_{jk} = 0$ for all others), and q_j may be substituted by its unbiased FRPFM measurement q_j^* at that intersection (the respective θ_j is assumed to be measured error free). This results in an unbiased transect discharge estimator

$$\rho_j^* = q_j^*\frac{A_T\omega_k}{L_k\cos\theta_j} \quad (6)$$

for a single intersection, i.e., ρ_j^* is the discharge estimate for the transect if only a single trace intersection was observed. In equation (6) transect area A_T, weights ω_k, and FRPFM lengths L_k are specified, and q_j^* and θ_j are obtained from FRPFM observation. In what follows, the relationship $q_j^* = q_j\Delta q_j$ is used, where Δq_j is assumed to be a positive

random variable of unit expectation (unbiasedness), and which accounts for local flux variability within individual traces in addition to the FRPFM flux measurement errors. The multiplicative nature of Δq_j (as opposed to additive, for example) is in concordance with the common use of percentages for measurement errors and also reflects the intuitive expectation that flux variability inside traces is proportional to the magnitude of the average trace flux (constant CV rather than constant standard deviation).

2.4. Discharge Estimator for Multiple Intersections

[17] In reality and as illustrated by Figure 4b, multiple intersections of traces with FRPFMs will occur possessing different fluxes q_j^* and orientations θ_j. Since discharges (and their estimates) are additive and since sums of Poisson processes again resemble Poisson processes of added densities [*Kingman*, 1993], ρ_j^* of equation (6) may be computed for each intersection and added together. This leads to an unbiased estimate Q^* of total transect discharge Q_a as

$$Q^* = \sum_{j=1}^{N_{\mathrm{PFM}}} \rho_j^* = A_T \sum_{k=1}^{N_{\mathrm{well}}} \frac{\omega_k}{L_k} \sum_{j=1}^{N_k} \frac{q_j^*}{\cos\theta_j}, \tag{7}$$

where N_k denotes the number of trace intersections for the kth FRPFM, and $N_{\mathrm{PFM}} = \sum_{k=1}^{N_{\mathrm{well}}} N_k$ represents the total number of intersections for all FRPFMs together. For rectangular transects of width W and height H, where all FRPFMs are of length H, $\rho_j^* = q_j^* \frac{W\omega_k}{\cos\theta_j}$ and when these FRPFMs are also evenly spaced, then $\rho_j^* = q_j^* \frac{W}{N_{\mathrm{well}}\cos\theta_j}$. It may be seen that ρ_j^* (and Q^*) for these two cases are independent of H, which is indirectly accounted for through the fact that N_{PFM} grows with H. Perhaps more interesting is that equation (7) is independent of local trace midpoint densities and trace length distributions. This is quite fortunate because information about these parameters is generally not available from borehole measurements. It results from a combination of two facts. (1) The expectation of true discharge (equation (3)) is a function of the product $\lambda_j\mu_{tj}$ between trace density and the expectation of trace length integrated over A_T. (2) This integral may be directly estimated by the number of intersections observed along the FRPFMs (equations (4) and (5)), without generally unavailable knowledge about the individual factors λ_j and μ_{tj} at all locations. For the same reason, equation (7) inherently accounts for the possibility of single traces intersecting more than one FRPFM. That is, the virtually impossible task of identifying intersections at multiple FRPFMs caused by one and the same trace is not required (each intersection is simply included in the summation of equation (7)). After all, it does not matter for transect discharge and total number of intersections whether the same fluxes are conveyed through many short traces (each causing at most one intersection) or through few long traces (each causing multiple intersections). The fact that Q^* does not require trace length also implies that possible correlations between trace length and trace flux (e.g., longer traces are expected to be better connected and hence may tend to convey larger fluxes) do not affect the estimator or its unbiasedness. For a given density, the number of intersections is proportional to trace length (equation (4)) and if longer traces are associated with larger (or smaller) fluxes, then this will be reflected in the frequency of observed values of q_j^*.

3. Validation of Unbiasedness and Assessment of Estimation Uncertainty

3.1. Monte Carlo Simulation

[18] It appears possible to use the second-order properties of Poisson processes (i.e., mean, variance, covariance) [*Kingman*, 1993] to analytically verify unbiasedness of equation (7) with respect to Q (recall that Q^* was derived as an unbiased estimator for Q_a) and to develop expressions for estimation variances. However, this task may become quite cumbersome for arbitrary trace orientations or more than a single FRPFM, and as an alternative, a numerical Monte Carlo (unconditional stochastic simulation) approach is adopted here. The approach is two-dimensional (in the plane of the transect) and does not involve any hydraulic modeling. In most general terms, it consists of the following procedure: before realizations can be generated, the size of the simulation domain has to be defined. For given transect dimensions, the simulation domain needs to extend sufficiently far in all directions beyond the transect limits, such that the portion of traces that could intersect the transect (i.e., contribute to Q and/or Q^*), but are not simulated because their midpoints lie outside the simulation domain, is zero or sufficiently small. For trace length distributions with finite upper bounds and arbitrary trace orientations, this may be achieved by extending the simulation domain by a distance equal to half the upper trace length bound beyond all sides of the transect. For unbounded trace length distributions (e.g., exponential or log-normal), this distance may be defined as half of a large enough quantile (99th percentile in the present work), such that the probability of not simulating a relevant trace is negligible without unnecessarily inflating computation times. Once the size of the simulation domain is defined, it remains constant for all realizations, which result from repeating the following steps:

[19] 1. Determine the number of trace midpoints in the simulation domain. It is a random number obtained from a Poisson distribution [*Kingman*, 1993] with expectation equal to $\int_{A_S} \lambda_j \mathrm{d}A$, where A_S is the area of the simulation domain.

[20] 2. Locate all trace midpoints across the simulation domain by randomly picking y and z coordinates from respective distributions (e.g., uniform distributions with upper and lower bounds equal to the y and z coordinates of the simulation domain limits if λ_j is constant).

[21] 3. Assign trace lengths, orientations, and trace average fluxes to all midpoints by randomly drawing from respective probability distributions (or one joint distribution), which may be a function of y and/or z.

[22] 4. Evaluate equation (1) to obtain one realization of the true discharge Q.

[23] 5. Take virtual FRPFM measurements by determining the intersections with traces and recording the respective trace orientations and trace average fluxes q_j (representing the sum of a possible smooth trend function and random flux variability between traces). Draw Δq_j (representing

within-trace flux variability and measurement error) from a positive random distribution of unit expectation to obtain observed fluxes as $q_j^* = q_j \Delta q_j$. Evaluate equation (7) to generate one realization of the discharge estimate Q^*.

[24] Denoting by M a large number of realizations and using $m = 1, 2, \ldots, M$ as an index for individual realizations, steps 4 and 5 deliver pairs of values Q_m and $Q^*{}_m$, which result in an estimation error $e_m = Q^*{}_m - Q_m$ for each realization. Over a large number of realizations, e_m populate a distribution with mean μ_e and variance $\sigma^2{}_e$ given by

$$\mu_e = \frac{1}{M}\sum_{m=1}^{M} e_m \tag{8}$$

$$\sigma_e^2 = \frac{1}{M}\sum_{m=1}^{M} (e_m - \mu_e)^2. \tag{9}$$

The expectation μ_Q of true discharge is obtained as

$$\mu_Q = \frac{1}{M}\sum_{m=1}^{M} Q_m \tag{10}$$

If the relative mean estimation error μ_e/μ_Q approaches zero as M increases, then the estimator is unbiased, i.e., the expectation of its estimation error is zero.

3.2. Normalization

[25] Since investigating a large number of possible parameter combinations through this procedure is impractical, attention is limited hereafter to rectangular transects, and the following normalizations are applied to subsequently generalize the outcomes of the Monte Carlo simulation as much as possible:

[26] 1. Transect and traces are scaled to unitary transect width and height ($W = H = 1$).

[27] 2. Trace midpoint density is adopted for unitary expectation of FRPFM-trace intersection ($\mu_{Nj} = \sum_{k=1}^{N_{\text{well}}} \mu_{Njk} = 1$).

[28] 3. Flux variability within traces and measurement errors are zero ($q_j^* = q_j$).

[29] 4. Trace average fluxes in the normalized domain are the same for all traces but may be of arbitrary value (zero between-trace flux variability, i.e., $q_j = \text{constant}$).

[30] The geometric scaling of a real-world transect and its traces to $W = H = 1$, such that the number of intersections and the portions of traces contributing to Q and Q_a remain unaffected, is simply a division of all y coordinates by W and all z coordinates by H. This leads to normalized horizontal and vertical trace length components of $\tau_y = t_j \cos\theta_j/W$ and $\tau_z = t_j \sin\theta_j/H$ resulting in a normalized trace length $\tau = \sqrt{\tau_y^2 + \tau_z^2}$ of

$$\tau = t_j \sqrt{\left(\frac{\cos\theta_j}{W}\right)^2 + \left(\frac{\sin\theta_j}{H}\right)^2}. \tag{11}$$

In a similar way, the normalized trace orientation $\vartheta = \arctan(\tau_z/\tau_y)$ is found as

$$\vartheta = \arctan\left(\frac{W}{H}\tan\theta_j\right). \tag{12}$$

It is seen that equations (11) and (12) reduce the number of variables from four (t_j, θ_j, W, H) to two (τ, ϑ). Furthermore, in order to achieve a unitary expectation of intersection, λ_j is divided by $\mu_{Nj} = \cos\theta_j \sum_{k=1}^{N_{\text{well}}} \int_{L_k} \lambda_j \mu_{tj} \mathrm{d}L$ representing the nonnormalized expected number of intersections for all FRPFMs together (sum of equation (4) over all FRPFMs). After multiplication by transect area WH to compensate for the geometric scaling, a normalized trace density λ_{norm} is obtained as

$$\lambda_{\text{norm}} = \lambda_j \frac{WH}{\mu_{Nj}} = \frac{W}{N_{\text{well}}\,\mu_{tj}\cos\theta_j} = \frac{1}{N_{\text{well}}\,\mu_\tau \cos\vartheta}. \tag{13}$$

The second expression applies when λ_j and μ_{tj} are constant in space, and all N_{well} FRPFMs are of equal length H. The final equality explores the geometric scaling relationships to express λ_{norm} in terms of normalized trace length and orientation. Normalization to $\mu_{Nj} = 1$ is convenient because it allows application of simulation results to ρ_j^* from equation (6), which eliminates N_{PFM} in equation (7) as a variable. Normalization to $q_j^* = q_j$ further eliminates Δq_j, and $q_j = \text{constant}$ (e.g., one) reduces the problem to estimating the cumulative trace length inside a transect from the number and orientations of intersections observed along the FRPFMs. Note that the particular value of q_j adopted does not affect the dimensionless mean estimation error μ_e/μ_Q or the dimensionless uncertainty measure CV_e used in the sequel. Relationships for generalizing normalized Monte Carlo simulation results to arbitrary values of N_{PFM} and variability in q_j and Δq_j are given subsequently.

3.3. Simulation Results Under Normalized Conditions

3.3.1. Evaluation of Estimator Unbiasedness

[31] Using the normalized conditions from above with a single FRPFM centered in a transect, Figure 5 shows four

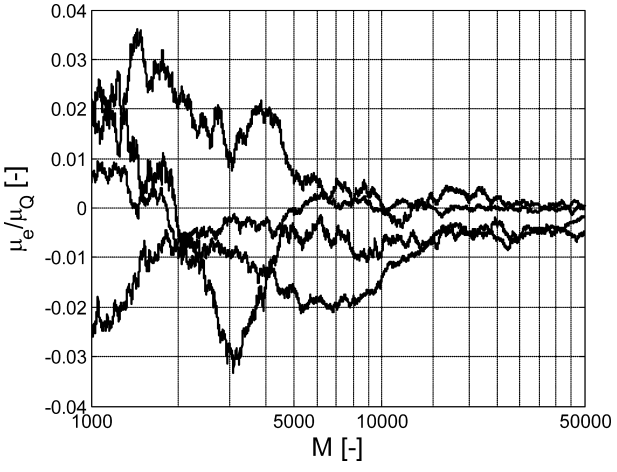

Figure 5. Arbitrary examples of convergence behavior of mean relative estimation error μ_e/μ_Q toward zero, as the number of realizations M increases (validation of unbiasedness). Chart is for $N_{\text{well}} = 1$ and normalized conditions, i.e., $W = H = \mu_{Nj} = q_j = q_j^* = 1$. Normalized trace length (equation (11)) and orientation (equation (12)) are constant for each case depicted and equal to $\tau = \{0.5, 1, 1.5, 2\}$ and $\vartheta = \{22.5°, 0°, 67.5°, 45°\}$.

arbitrary examples of how the mean relative estimation error μ_e/μ_Q converges toward zero as M grows. For each graph, trace density, length, and orientation are kept constant (across space as well as across realizations). The same convergence behavior (although not shown for brevity) is observed for all other scenarios investigated in subsequent figures. This validates the unbiasedness of estimator ρ_j^* of equation (6) for $q_j = q_j^* = \text{constant}$. Consequently, since Δq_j is independent of q_j and of unit expectation, and by the same reasoning leading from ρ_j^* to Q^* in equation (7) (i.e., additivity of true discharges, discharge estimates, and Poisson processes), this also validates the unbiasedness of Q^* with respect to true discharge Q from equation (1). The unbiasedness reflects that the expectations of equations (1) and (2) are identical, i.e., on average the trace portions inside the transect, which pertain to traces with midpoints outside the transect (Figure 3a), convey the same discharge as the trace portions outside the transect, which pertain to traces with midpoints inside the transect (Figure 3b). Since a transect of arbitrary shape may always be decomposed into a sum of arbitrarily small rectangles, this conclusion may be further generalized to arbitrary transect shapes.

3.3.2. Evaluation of Discharge Estimation Error

[32] For the same normalized conditions and no spatial trends in normalized trace density λ_{norm}, normalized trace length μ_τ, or trace average fluxes μ_q, Figure 6a represents the dimensionless estimation uncertainty in terms of a squared coefficient of error variation $\text{CV}^2{}_e = \sigma^2{}_e/\mu^2{}_Q$ obtained from equations (9) and (10) for a single FRPFM and $M = 50{,}000$. Bold continuous lines correspond to constant trace length, while dashed lines correspond to uniform (bounded between zero and $2\mu_\tau$) and thin continuous lines to exponential trace length distributions. Results for log-normal trace length distributions of $\text{CV} = 0.5$ and 1 are almost identical to those of uniform ($\text{CV} = 0.58$) and exponential ($\text{CV} = 1$) distributions, respectively (graphs not shown). Overall, it is seen that $\text{CV}^2{}_e$ decreases as traces become longer, which may be attributed to a higher degree of spatial continuity (less variability) between the measurement location (FRPFM) and the unsampled portion of the transect. Due to the same reasoning and in combination with the horizontally aligned transect, $\text{CV}^2{}_e$ increases as trace orientation deviates from the horizontal direction.

[33] For the distributions investigated it may also be consistently observed from Figure 6a that $\text{CV}^2{}_e$ for constant trace lengths ($\text{CV}^2{}_{e,\text{const}}$ hereafter) is always equal or larger than $\text{CV}^2{}_e$ for random trace lengths ($\text{CV}^2{}_{e,\text{rand}}$ hereafter). In fact, denoting the probability distribution of τ for a given ϑ by pdf(τ) it can be shown that (Appendix A)

$$\text{CV}^2{}_{e,\text{rand}} = \frac{1}{\mu_\tau}\int_0^\infty \text{CV}^2{}_{e,\text{const}}\,\text{pdf}\,(\tau)\tau\,\text{d}\tau, \tag{14}$$

which remains valid in the presence of spatially variable density and spatially variable trace length expectation (τ and μ_τ are then taken with respect to some reference point). Equation (14) reflects that $\text{CV}^2{}_{e,\text{rand}}$ is nothing but a weighted and rescaled average of $\text{CV}^2{}_{e,\text{const}}$. The weighting function pdf(τ)τ accounts for the likeliness of a trace length τ to occur and compensates for the inversely proportional dependency of trace density on trace length used in Figure 6

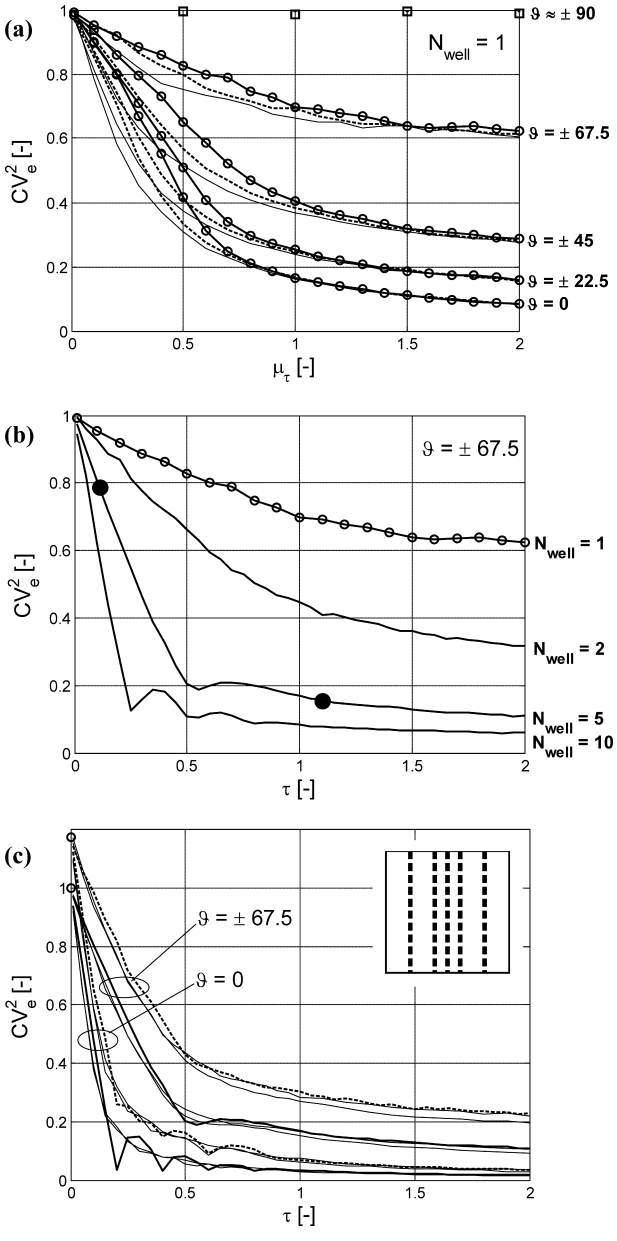

Figure 6. $\text{CV}^2{}_e$ as a function of normalized trace length under different scenarios and for $M = 50{,}000$. (a) No spatial trends in λ_{norm}, μ_τ, or μ_q and trace length constant (bold continuous), uniformly distributed (dashed), and exponentially distributed (thin continuous). Squares are for constant trace length and $\vartheta = 89°$, and circles indicate the resolution used for μ_τ. (b) No spatial trends in λ_{norm}, μ_τ, or μ_q and uniformly spaced wells. Constant trace length $\tau = \mu_\tau$ and bold dots are for practical example. (c) No spatial trend in μ_q, constant trace length $\tau = \mu_\tau$, and five irregularly spaced FRPFMs (locations shown as dashed lines in upper right corner). Dashed graphs are for no spatial trend in μ_τ. Bold continuous lines are for five evenly spaced FRPFMs given for comparison (as in (b)). For linearly varying trace density (from zero to a maximum value over simulation domain), graphs fall on top of bold continuous and dashed lines. Thin continuous lines correspond to linearly varying trace length $\tau = \mu_\tau$ (vertically and horizontally from zero to a maximum value over simulation domain with τ on abscissa at center of transect). Circles indicate $\text{CV}^2{}_{e,\text{max}}$ as obtained from the first expression of equation (18).

(due to normalization of equation (13)). The factor τ implies that lower values of $CV^2_{e,const}$ corresponding to longer traces receive larger weights leading to $CV^2_{e,rand} < CV^2_{e,const}$ for a given μ_τ. It is surmised that this relationship holds in rather general terms for symmetric and positively skewed (long tail to the right) trace length distributions. This means that $CV^2_e = CV^2_{e,const}$ may be used as a conservative worst case value (upper bound) in typical practical scenarios, where knowledge about trace length distributions is limited. The squares in Figure 6a show that $CV^2_{e,const}$ converges to one as ϑ approaches 90° (vertical traces). In this case $CV^2_{e,const}$ is not a function of τ anymore, and equation (14) immediately leads to $CV^2_{e,rand} = CV^2_{e,const}$ for arbitrary trace length distributions. In what follows attention is limited to $\tau = \mu_\tau$, which may follow a smooth spatial trend, however, and the notation CV^2_e is resumed as an abbreviation for $CV^2_{e,const}$.

[34] Figure 6b represents some results for CV^2_e (i.e., constant $\tau = \mu_\tau$) and evenly spaced FRPFMs in a rectangular transect (i.e., $\omega_k = 1/N_{well}$), where λ_{norm}, μ_τ, and μ_q are again constant across the transect. It is seen that CV^2_e decreases as the number of monitoring wells increases and that CV^2_e is not monotonic any more with τ. Due to the effect of correlation between the numbers of intersections at nearby FRPFMs, local minima occur, where horizontal projections of trace lengths reach multiples of well spacing (i.e., single traces begin to intersect two or more FRPFMs). However, by equation (14) these minima are smoothed out if trace length is random. Note in this context that it is generally not correct to divide a transect with multiple observation wells into portions, which contain a single well each, and to compute (e.g., from Figure 6a) and sum the estimation error variances for all portions. The reason for this is possible correlation between estimation errors of neighboring transect portions and possible underestimation of total estimation uncertainty.

[35] The dashed curves in Figure 6c represent examples of CV^2_e for five vertical, but irregularly spaced, FRPFMs (illustrated by dashed lines in upper right corner) and spatially constant λ_{norm}, μ_τ, and μ_q. The bold continuous lines are given for comparison and correspond to the same scenario, but even well spacing (as considered in Figure 6b). For all cases shown, a linear trend in trace density from zero to some maximum value over the simulation domain (as defined in section 3.1) does not affect the graphs of CV_e. Allowing trace length to follow the same spatial trend function (but keeping τ constant over realizations) yields the thin continuous graphs, which also closely follow the results for stationary conditions except for smoothing of local extrema. The same behavior is observed for other configurations investigated (e.g., nonsymmetric FRPFM arrangements), but not shown here for brevity. In general, this leads to the conclusion that even well spacing performs best in terms of minimizing CV^2_e.

3.4. Generalization of Results to Nonnormalized Conditions

[36] The observed unbiasedness of the discharge estimator under normalized conditions has already been generalized to arbitrary conditions by the argumentation above. In contrast, the estimation uncertainty contained in CV^2_e is only due to geometric factors, such as trace orientation and the spatial randomness of trace locations and lengths. Uncertainty due to flux variability between and within traces as well as due to the measurement errors is still to be included. Since graphs of CV^2_e in Figure 6 are for an expected number of trace intersections $\mu_{Nj} = 1$, values of CV^2_e may be directly applied to ρ^*_j from equation (6) for arbitrary $q^*_j = q_j$ (i.e., $\Delta q_j = 1$ as used for computation of CV^2_e). That is, charts in Figure 6 are normalized such that a specific value of CV^2_{ej} may be applied to a particular intersection of flux q_j and orientation θ_j recorded on a FRPFM to deliver an estimation error variance of $\sigma^2_{ej} = CV^2_{ej}\rho^2_j$, where $\rho_j = q_j A_T \omega_k / L_k \cos\theta_j$ in analogy to equation (6). Now allowing for $\Delta q_j \neq 1$ and denoting its CV by CV_Δ, it is known that Δq_j causes an additional variance of $CV^2_\Delta \rho^2_j$ in estimator ρ^*_j, while not affecting the true discharge. Since Δq_j represents within-trace flux variability and FRPFM measurement errors, it is also independent of all other processes involved, and its variance may be simply summed to the estimation error variance for $\Delta q_j = 1$ giving a generalized $\sigma^2_{ej} = \rho^2_j(CV^2_{ej} + CV^2_\Delta)$ for a discharge estimate based on a single intersection (equation (6)). Moreover, since CV^2_{ej} is computed for the exact number and arrangement of FRPFMs in a transect, it accounts for possible correlations between discharge estimates (and hence estimation errors) from neighboring FRPFMs. Thus, the same principle of additivity of discharges and Poisson processes that led from equation (6) to equation (7) may be applied. In combination with Δq_j stemming from an independent process, this means that the estimation error variances for single intersections may be added up to a total discharge estimation error variance $\sigma^2_{e,PFM} = \sum_{j=1}^{N_{PFM}} \sigma^2_{ej}$ of Q^* resulting as

$$\sigma^2_{e,PFM} = \sum_{j=1}^{N_{PFM}} \rho^2_j (CV^2_{ej} + CV^2_\Delta), \tag{15}$$

where subscript "PFM" with σ^2_e indicates validity for all traces in the transect. However, as opposed to equation (7), direct evaluation of equation (15) is complicated by three factors: (1) although measured ρ^*_j are unbiased estimates of ρ_j, ρ^{*2}_j are not unbiased estimates of ρ^2_j (estimation of $\rho_j\rho_j$ by $\rho^*_j\ \rho^*_j$ violates the condition of uncorrelatedness between unbiased estimators ρ^*_jandρ^*_j, or in other words, the expectations of ρ^{*2}_j and ρ^2_j are not the same); (2) CV_Δ is unknown because of unknown magnitude of within-trace flux variability; and (3) CV^2_{ej} depends on generally unknown trace length parameters.

3.5. Upper Uncertainty Bounds

[37] One way to overcome this problem is to limit attention to trace sets of constant orientation (all other variables including fluxes remain random), for which the subscript "set" is used in the sequel. Note that grouping fractures or traces into sets of (approximately) constant orientation is a common procedure in fractured rock characterization. Thus, as derived in Appendix B, a $CV^2_{e,set}$ for set discharge uncertainty may be obtained as

$$CV^2_{e,set} = \frac{\left(1 + CV^2_\rho\right)\left(CV^2_e + CV^2_\Delta\right)}{N_{set}}, \tag{16}$$

where N_{set} is the number of intersections caused by the trace set, CV_e is the normalized estimation uncertainty for the trace set orientation, CV_ρ is the variability of trace average fluxes ρ_j, and CV_Δ is the variability Δq_j of fluxes within traces of the set including random measurement errors. Similar to equation (15), evaluation of equation (16) is still complicated in practice by the fact that CV_ρ, CV_e, and CV_Δ have to be known. However, as further shown in Appendix B an upper bound of $CV^2_{e,set}$ may be found as

$$CV^2_{e,set} \le \frac{\left(1 + CV^2_e + CV^2_{\rho*}\right)^2}{4N_{set}}, \qquad (17)$$

where CV_{ρ^*} is the variability of FRPFM observed fluxes ρ^*_j. Intuitively speaking, this means that while the individual magnitudes of CV^2_ρ and CV^2_Δ in equation (16) are not known in field situations, $CV^2_{\rho^*}$ is in fact obtained by FRPFM measurements and allows finding the upper bound of $CV^2_{e,set}$ in equation (17). While N_{set} is also known from FRPFM measurements, the remaining problem is to determine CV_e if properties of trace length distribution are not available.

[38] Helpful in this respect is Figure 6, which illustrates that CV_e consistently approaches a maximum value $CV_{e,max}$ if the trace length expectation μ_τ goes to zero. By equation (14) $CV_{e,max}$ is independent of a particular trace length distribution (i.e., $CV^2_{e,rand} = CV^2_{e,const}$), since with μ_τ the variability in τ also has to go to zero to maintain nonnegativity. As derived in Appendix C $CV_{e,max}$ may be found from

$$CV^2_{e,max} = 1 + CV'^2_{\omega/L} = \frac{\frac{1}{N_{PFM}}\sum_{k=1}^{N_{well}} N_k \left(\frac{\omega_k}{L_k}\right)^2}{\left(\frac{1}{N_{PFM}}\sum_{k=1}^{N_{well}} N_k \frac{\omega_k}{L_k}\right)^2}, \qquad (18)$$

where $CV'^2_{\omega/L}$ denotes the CV of the ratio ω_k/L_k after weighting by the expected numbers of intersections per FRPFM. The first equality is validated by the circles on the ordinate of Figure 6c and for further cases investigated, but not shown for brevity. The last expression in equation (18) is important for practice, as it allows estimating $CV^2_{e,max}$ from FRPFM measured parameters. It inherently accounts for possible spatial trends in trace density and/or length through the observed number of intersections N_k per FRPFM. In the absence of information about trace length for determination of CV_e from the Monte Carlo simulation under normalized conditions, $CV_{e,max}$ may be used instead of CV_e in equation (16) or (17) to obtain a conservative upper bound of uncertainty about a trace set discharge estimate from equation (7). The only requirement for evaluation of equation (17) is then that N_{set} be large enough for a reliable determination of set specific $CV^2_{\rho^*}$.

[39] Since $CV_{e,max}$ does not depend on trace orientation, it may also be directly plugged into equation (15) instead of CV_{ej}, and by the same manipulations leading to equation (17), a general upper bound for discharge uncertainty independent of individual trace orientations is obtained as

$$CV^2_{e,PFM} \le \frac{\left(1 + CV^2_{e,max} + CV^2_{\rho*}\right)^2}{4N_{PFM}} \approx \frac{1 + CV^2_{\rho*} + \frac{CV^4_{\rho*}}{4}}{N_{PFM}}, \qquad (19)$$

where the final equality is exact when $\omega_k/L_k = \text{constant}$ ($CV_{e,max} = 1$) as it is the case for evenly spaced FRPFMs of equal lengths. However, it is expected that the contribution of variability in ω_k/L_k through the term $CV'^2_{\omega/L}$ in equation (18) is rather negligible with respect to the transformed flux variability $CV^2_{\rho*}$, such that the final equality in equation (19) may be regarded as an accurate approximation in general. For the configuration of Figure 6c $CV^2_{e,max} = 1.18$, for example, and the approximation errors amount to 6% and 3% for $CV_{\rho^*} = 1$ and 2, respectively.

[40] Of considerable interest are also the capabilities of equations (16), (17), and (19) to predict uncertainty reduction due to additional sampling. For example, given $CV^2_{e,PFM}$ is the upper uncertainty bound obtained for N_{PFM} intersections at N_{well} FRPFMs, each additional FRPFM installed may be expected to increase N_{PFM} by N_{PFM}/N_{well} intersections (assuming stationary conditions across the transect). Doubling N_{well}, for instance, may be expected to double N_{PFM} and halve $CV^2_{e,PFM}$ (i.e., reduce confidence interval width by a factor of $\sqrt{2}$) under the hypothesis that μ_{ρ^*} and $CV^2_{\rho^*}$ are not significantly affected by the additional sampling. Since the worst case scenario occurs when traces are very short, such that spatial correlations among measured fluxes and with transect discharge are eliminated, this result is identical to the "standard error equation" for mean estimates in classical statistics for identically and independently distributed random variables. Future FRPFM sampling locations may be optimized by attempting to minimize $CV_{e,PFM}$ through (1) minimizing $CV_{e,max}$ in equation (18) by locating FRPFMs as uniformly as possible, and through (2) locating additional FRPFMs in areas of high probability of intersection to maximize N_{PFM}.

4. Validation and Example

[41] This section assumes trace properties as well as CV_ρ and CV_Δ are known, such that equation (16) may be validated. Shown in Figures 7 and 8 are examples of outcomes

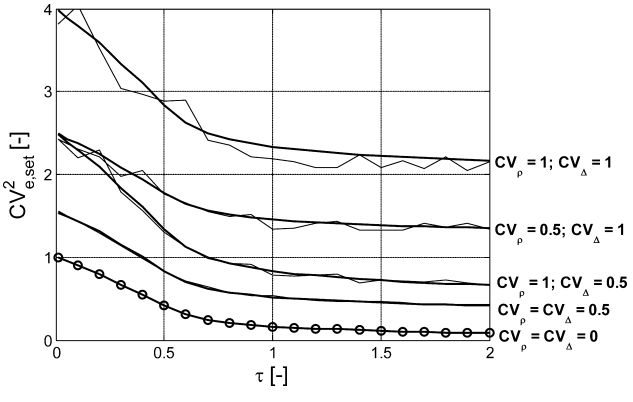

Figure 7. $CV^2_{e,set}$ for $N_{well} = 1$ and $\vartheta = 0$ as a function of constant trace length $\tau = \mu_\tau$ and for different combinations of CV_ρ (variability of trace average fluxes) and CV_Δ (variability of within-trace fluxes plus FRPFM measurement error). Bold line with circles is from Figure 6a; simple bold lines are from equation (16) with $N_{set} = 1$; and thin lines are from running direct Monte Carlo simulations with $\mu_{Nj} = 1$ and the values of CV_ρ and CV_Δ indicated ($M = 5000$). No spatial trends in λ_{norm}, μ_τ or μ_q.

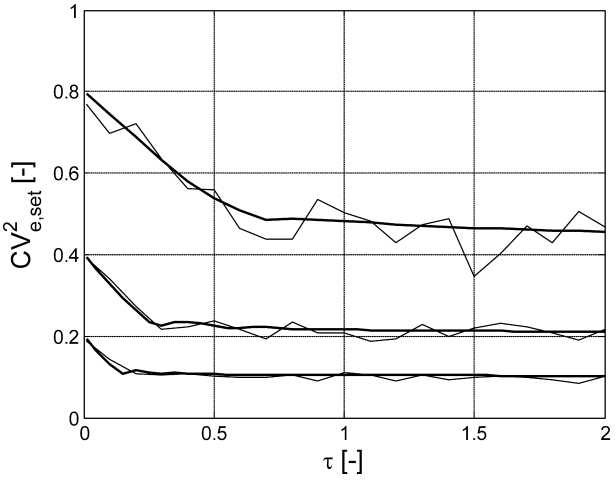

Figure 8. $CV^2_{e,set}$ for evenly spaced wells, $CV_\rho = CV_\Delta = 1$ and $\vartheta = \pm 45°$ as a function of constant trace length $\tau = \mu_\tau$. (top) $N_{well} = 2$, $\mu_{Nj} = 5$, and linear vertical trend in trace density. (center) $N_{well} = 5$, $\mu_{Nj} = 10$, and linear horizontal trend in trace density. (bottom) $N_{well} = 10$, $\mu_{Nj} = 20$, and linear vertical trend in trace length. Bold continuous lines are from CV^2_e (similar to Figure 6b) in combination with equation (16). Thin continuous lines are from the Monte Carlo simulation directly using the respective parameters and $M = 5000$.

of equation (16) (bold lines) in comparison to results from direct (i.e., not normalized) Monte Carlo simulation (thin lines). Figure 7 is for a single vertical FRPFM centered within a transect and for different combinations of CV_ρ and CV_Δ. Trace orientation is kept constant at $\vartheta = 0$ and $N_{set} = 1$. In Figure 8 $\vartheta = \pm 45°$ with $CV_\rho = CV_\Delta = 1$, where FRPFMs are evenly spaced with $N_{well} = \{2, 5, 10\}$ and expected number of intersections $\mu_{Nj} = \{5, 10, 20\}$ from top-down. Different linear trends in trace density or trace length are applied to each case. Figure 9 uses the same parameters and trend functions as Figure 8, except for an additional bell-shaped trend function superimposed on trace average fluxes to generically emulate a contaminant

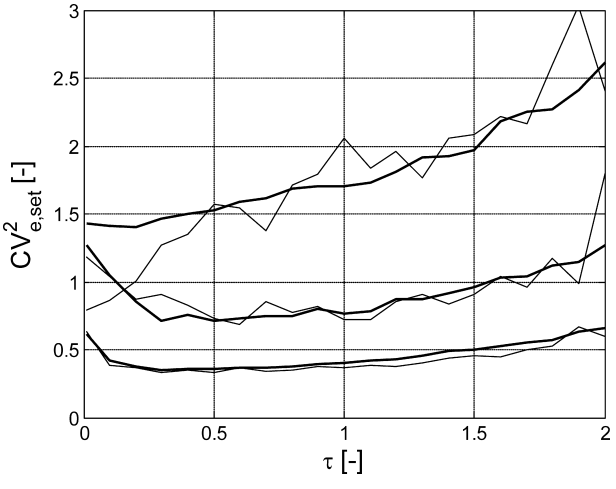

Figure 9. Same as Figure 8, but including a bell-shaped trend function (generic plume), which increases magnitude of between-trace flux variability ($M = 50{,}000$).

plume. Without loss of generality, this only aims at reproducing the most fundamental qualitative features of a contaminant plume (decreasing fluxes from center to periphery) and does not attempt to resemble a fractured rock plume in all complexity. In the normalized transect centered at the origin of the coordinate system, this trend function is chosen as $\exp[-20(\tau^2_x + \tau^2_y)]$, which is a simple smooth function with a maximum at the origin that decays to less than 1% of its peak value near the transect limits. For all traces the trend function is evaluated at their midpoints and used to multiply their trace average fluxes q_j before evaluating equations (8)–(10). The presence of a plume significantly increases the variability in measured fluxes (compare example below).

[42] In all cases, convergence of Monte Carlo simulation results with increasing number of realizations toward equation (16) is confirmed. It is observed, however, that the number $M = 50{,}000$ of realizations used in each data point of Figure 9, for example, may still be too small if N_{set} is small in combination with large CV_ρ and CV_Δ. This is reflected by the variability in the thin lines about the bold lines. Equation (16), hence, also represents an effective shortcut to otherwise lengthy (at the order of 30 min for some charts) numerical computations, especially for long traces (large simulation domain) and large flux variability (slow convergence). Figures 7–9 use a constant trace length $\tau = \mu_\tau$ over realizations, and the conclusions may be generalized to other trace length distributions by applying equation (14) to CV_e before evaluating equation (16). Validation of equation (14) was performed separately using graphs from Figure 6a, but results are not shown for brevity. Similar as with equation (5), however, it is pointed out that the measured CV_{ρ^*} has to reliably reflect the actual degree of flux variability over the transect in order to avoid uncontrolled biases in discharge and uncertainty estimates. This may be warranted by deploying a sufficient number of evenly spaced FRPFMs. Alternatively, for unevenly spaced FRPFMs, the constants ω_k may again be regarded as a kind of declustering weights, which work toward achieving this representativeness. A distinct feature in Figure 9 is the increase in $CV_{e,set}$ with longer traces. This was found to be a pure consequence of the trend function imposed on fluxes and the fact that trace average flux variability CV_ρ inside the transect increases with trace length (traces further outside the transect may still contribute to Q and/or Q^*, thus increasing the degree of variability in the transect).

[43] In order to illustrate a practical application of the present results and as a further validation, an example problem for a hypothetical field situation is presented. Table 1 summarizes the relevant parameters used, and Figure 4b illustrates one out of 5000 realizations used with a transect of 5 m × 20 m and five evenly spaced FRPFMs. Note the fact that larger μ_t associated with larger μ_q implies positive correlation between trace length and trace average flux when regarding both trace sets together. Table 2 considers water discharge (i.e., assuming no spatial trend in fluxes) and summarizes results for each trace set separately as well as for the combination of both. Equations (8)–(10) are used to validate unbiasedness ($\mu_e/\mu_Q \ll 1$) and to assess "true" estimation uncertainty denoted by $CV_{e,sim}$ (i.e., error CV from simulation for nonnormalized conditions). To all realizations, each of which could correspond to actual field and

Table 1. Parameters for Example Problem With Illustration of a Single Realization Given in Figure 4b[a]

Trace Set	λ (1/m^2)	μ_t[b] (m)	θ[c] (°)	μ_q[d] (m^2/d)	CV$_\rho$[d]	CV$_\Delta$[d]	μ_τ[e]	ϑ[e](°)	μ_N[f]	CV$_e$[g]
1	0.15	10	−35/−25	0.3	0.5	0.5	1.1	−67	32.5	0.40
2	2	1	20/40	0.1	0.75	0.5	0.1	67	43.3	0.89

[a]No spatial trends in trace density or mean trace length.
[b]Exponential distributions.
[c]Min/max of uniform distributions.
[d]Log-normal distributions.
[e]For average θ from equations (11) and (12).
[f]From applying equation (4) to each FRPFM and summation.
[g]From dots in Figure 6b (for constant trace length) and taking square root.

sampling conditions at a site, equations (16), (17), and (19) are also applied, and the outcomes are reported as averages over all realizations. CV$_{e,\mathrm{PFM}}$ from equation (19) only requires FRPFM measurable parameters CV$_{\rho^*}$ and N_{PFM} and correctly delivers upper uncertainty bounds on the discharge estimates (CV$_{e,\mathrm{PFM}} >$ CV$_{e,\mathrm{sim}}$). If additional information is available regarding trace lengths (e.g., from nearby outcrops), CV$_e$ may be determined and used in equation (17) to tighten the upper uncertainty bounds. In the less likely event of given knowledge about the distribution of flux variability between and within traces, equation (16) may be evaluated, which is seen to closely approximate CV$_{e,\mathrm{sim}}$ in all cases. It is further evident that the upper uncertainty bounds for trace set 2 are tighter (i.e., closer to the "true" value CV$_{e,\mathrm{sim}}$) than those of trace set 1, which is due to a larger value of CV$_e$ and more "closeness" to the worst case scenario. All of the above observations are confirmed by Table 3, which corresponds to the same scenario of Tables 1 and 2, except for the presence of a bell-shaped trend in trace average fluxes as used with Figure 9 (note that this also applies to trends in trace orientation, since by equation (6), it does not matter whether a trend in ρ^* is due to a trend in q or θ). If this trend function is given the units of contaminant concentration, then q and q^* become contaminant mass fluxes with significantly higher CVs (compare CV$_\rho$ and CV$_{\rho^*}$ between Tables 2 and 3), which further propagates into larger discharge uncertainties.

5. Summary and Conclusion

[44] The present work develops and validates an estimator for water and/or contaminant discharges across transects (control planes) in fractured rock aquifers. The method is based on FRPFM measurements of local fracture fluxes along monitoring wells contained inside a transect. Fracture traces (i.e., intersections of fracture planes with the transect plane) are conceptualized as straight lines of random location, length, and orientation. The components contributing to variability in measured fluxes are due to (1) smooth trend functions (e.g., plume shape), (2) variability of trace average fluxes, (3) variability of local fluxes within traces, and (4) random measurement errors. The estimator Q^* (equation (7)) only requires measured trace fluxes and orientations and is found to be unbiased under quite general conditions including the presence of linear trends in trace density or trace length across the transect. Particular knowledge about trace density and random trace length properties, however, is not required for estimating transect discharge. Discharge estimation uncertainty is derived in terms of a distribution independent error CV by using a numerical Monte Carlo simulation approach under normalized conditions with subsequent analytical generalization. Uncertainty is found to depend on generally unknown trace length distributions (especially trace length expectations) and the relative contributions of between- and within-trace flux variabilities (equation (16)). For practical use, an equation is developed, which delivers an upper bound for discharge uncertainty based on the FRPFM measurable variables only (equation (19)). Equation (16) is successfully validated against direct Monte Carlo simulation results for a variety of scenarios including multiple vertical and unevenly spaced FRPFMs and the presence or not of a bell-shaped trend function in fluxes (generic plume example) across a transect. An example problem further demonstrates the application and performance of the discharge estimator and its equations for uncertainty assessment.

[45] The approach, even though partly numerically based, does not involve any hydromechanical flow or

Table 2. Results of Example Problem Defined in Table 1 and Figure 4b for Water Discharge (No Spatial Trend in Fluxes) Based on 5000 Realizations[a]

Trace Set	CV$_\rho$	CV$_{\rho^*}$[b]	μ_Q[c] (m^3/d)	μ_e/μ_Q[c]	CV$_{e,\mathrm{sim}}$[c]	CV$_{e,\mathrm{PFM}}$[d]	CV$_{e,\mathrm{set}}$[e]	CV$_{e,\mathrm{set}}$[f]
1	0.48	0.71	44.9	−0.0003	0.12	0.23	0.15	0.13
2	0.72	0.91	20.0	0.003	0.18	0.22	0.21	0.20
1 + 2	0.80	1.00	64.9	0.0007	0.10	0.18	0.12[g]	0.11[g]

[a]CVs are computed for each realization and then averaged over all realizations.
[b]Using equation (6).
[c]From equations (8)–(10) without normalization of simulation parameters.
[d]From equation (19).
[e]From equation (17).
[f]From equation (16).
[g]Using $[(Q^*_1 \mathrm{CV}_{e,\mathrm{set},1})^2 + (Q^*_2 \mathrm{CV}_{e,\mathrm{set},2})^2]^{1/2}/(Q^*_1 + Q^*_2)$ to combine sets and subsequent averaging over all realizations.

Table 3. Results of Example Problem Defined in Table 1 and Figure 4b for Contaminant Discharge (With Same Spatial Trend in Fluxes as Used With Figure 9 in g/m^3) Based on 5000 Realizations[a]

Trace Set	CV_ρ	CV_{ρ^*}[b]	μ_Q (g/d)[c]	μ_e/μ_Q[c]	$CV_{e,sim}$[c]	$CV_{e,PFM}$[d]	$CV_{e,set}$[e]	$CV_{e,set}$[f]
1	2.14	2.29	4.3	0.005	0.27	0.67	0.60	0.27
2	1.84	1.99	3.1	0.005	0.31	0.47	0.47	0.34
1 + 2	2.18	2.37	7.4	0.005	0.21	0.45	0.41[g]	0.22[g]

[a]Footnotes as in Table 2.

transport modeling. It rather takes advantage of directly measured fracture fluxes (readily integrated over fracture aperture) produced by the in situ hydrogeological conditions. Consequently, fundamental parameters such as fracture aperture or piezometric gradient are irrelevant. However, it is a fundamental requirement that sufficient fracture fluxes be sampled, such that measured flux variability CV_{ρ^*} reliably represents the actual degree of flux variability across the transect. This condition may be verified by observing no further increase in CV_{ρ^*} as the number of sampled fluxes grows. Assuming an observed value of $CV_{\rho^*} = 1$ and a target value of $CV_{e,PFM} < 0.3$ (i.e., the interval of plus/minus one standard deviation equal to 30% of the discharge estimate contains the true discharge with a probability of larger than 68% under an assumption of normality), equation (19) shows that $N_{PFM} \geq 25$ trace flux measurements (intersections) are necessary. For $CV_{q^*} = 2$ the required N_{PFM} would increase to 100, which may again be lowered if information about average trace length (or a lower bound thereof) is available, for example. Equations (6) and (19) also demonstrate that a number of vertical FRPFMs are not appropriate for estimating discharges through near vertical trace sets, where $\cos\theta_j$ is very small, thus inflating CV_{ρ^*} and at the same time limiting $N_{PFM.}$ While not discussed here, it appears possible, however, to apply the present approach to nonvertical and nonparallel FRPFMs to circumvent this problem. Finally, results are directly applicable to other borehole investigation methods, which provide measurements of local fracture fluxes and orientations (e.g., visual or high-resolution thermal detection of trace locations and orientations for subsequent performance of a localized borehole dilution test) [*Pehme et al*., 2010; *Novakowski et al*., 2006]. If the measured magnitudes are not fluxes, but contaminant concentrations (e.g., from the method of *Cherry et al*. [2007]), then the present approach allows estimating the transect average concentration associated with a respective uncertainty bound (this generally holds for any linearly averaging parameter).

Appendix A: Derivation of $CV_{e,rand}$ (Equation (14))

[46] Denoting the probability distribution of τ for a given ϑ by pdf(τ) and exploring additivity of variances of Poisson processes leads to a variance $\sigma^2_{e,rand}$ of

$$\sigma^2_{e,rand} = \frac{\int_0^\infty \sigma^2_{e,const}\frac{\text{pdf}(\tau)}{\lambda_{norm}}d\tau}{\int_0^\infty \frac{\text{pdf}(\tau)}{\lambda_{norm}}d\tau} = \frac{\int_0^\infty CV^2_{e,const}\mu^2_{Qaj,const}\,\text{pdf}(\tau)\tau d\tau}{\int_0^\infty \text{pdf}(\tau)\tau d\tau}, \quad \text{(A1)}$$

where $\sigma^2_{e,const}/\lambda_{norm} = CV^2_{e,const}\mu^2_{Qaj,const}/\lambda_{norm}$ is the estimation error variance for a constant trace length and unit normalized density (instead of unit expectation of intersection). For the final equality, use is also made of the last expression of equation (13) with $\mu_\tau = \tau$. The integral in the denominator of the first equality in equation (A1) represents the expected number of intersections for unit normalized density and serves to rescale the numerator, such that $\sigma^2_{e,rand}$ again applies to a unit expectation of intersection (instead of unit normalized density). The constant number of intersections applied to arrive at equation (13) further implies that $\int_{L_k}\lambda_{norm}\tau dL = const$ for each FRPFM, such that $\int_{A_T}\lambda_{norm}\tau dA = const$ in equation (5). Equation (3) then shows that $\mu_{Qaj,const}$ is not a function of τ under normalized conditions, and in analogy to equation (A1) (except for using additivity of Poisson expectations), this leads to

$$\mu_{Qaj,rand} = \frac{\int_0^\infty \mu_{Qaj,const}\frac{\text{pdf}(\tau)}{\lambda_{norm}}d\tau}{\int_0^\infty \frac{\text{pdf}(\tau)}{\lambda_{norm}}d\tau} = \mu_{Qaj,const}. \quad \text{(A2)}$$

Division of equation (A1) by the square of equation (A2) leads to $CV^2_{e,rand}$ in equation (14), where $\mu_\tau = \int_0^\infty \text{pdf}(\tau)\tau d\tau$.

Appendix B: Derivation of $CV_{e,set}$ (Equations (16) and (17))

[47] For a trace set of constant orientation, CV^2_{ej} in equation (15) reduces to a constant value CV^2_e, and an estimation error variance $\sigma^2_{e,set}$ of N_{set} intersections may be written as $\sigma^2_{e,set} = \left(CV^2_e + CV^2_\Delta\right)\sum_{j=1}^{N_{set}}\rho_j^2$. Using μ_ρ and CV_ρ for expectation and CV of all ρ_j in a set, the expectation of ρ^2_j is known as $\mu^2_\rho\left(1 + CV^2_\rho\right)$. For a given N_{set} this translates into an expectation of $\sigma^2_{e,set}$ as $N_{set}\mu^2_\rho\left(1 + CV^2_\rho\right)\left(CV^2_e + CV^2_\Delta\right)$. At the same time, an estimator Q^*_{set} from equation (7) possesses the expectation $N_{set}\mu_{\rho*}$, where μ_{ρ^*} is the expectation of ρ_j^* from applying equation (6) to all measured fluxed of the trace set. Knowing that $\mu_{\rho^*} = \mu_\rho$ and dividing the expectation of $\sigma^2_{e,set}$ by the squared expectation of Q^*_{set} gives equation (16). Hereby, it is interesting to note that an arbitrary number of additional trace intersections with zero fluxes does not affect $\sigma^2_{e,set}$ nor Q^*_{set}, such that the synthetic addition of such "dummy data" does not affect the validity

of equations (7) and (16). Furthermore, exploring that $\rho_j^* = \rho_j \Delta q_j$, where ρ_j and Δq_j are independent, a CV of measured and transformed fluxes ρ_j^* is obtained as $\mathrm{CV}^2_{\rho^*} = \mathrm{CV}^2_{\rho} + \mathrm{CV}^2_{\Delta}$. Using this equality as a constraint, equation (16) may be maximized by setting $1 + \mathrm{CV}^2_{\rho} = \mathrm{CV}^2_{e} + \mathrm{CV}^2_{\Delta}$ (given the sum of two factors, their product is maximized when the factors are equal) to arrive at the upper bound for $\mathrm{CV}_{e,\mathrm{set}}$ given in equation (17).

Appendix C: Derivation of $\mathrm{CV}_{e,\mathrm{max}}$ (Equation (18))

[48] By definition of the estimation error $e_m = Q^* - Q$ in section 3.1, the estimation error variance of equation (9) is known to be equal to

$$\sigma_e^2 = \sigma_{Q^*}^2 + \sigma_Q^2 - 2\mathrm{Cov}\,(Q^*, Q), \tag{C1}$$

where $\sigma^2_{Q^*}$ and σ^2_Q are the variances of Q^* and Q, while $\mathrm{Cov}(Q^*,Q)$ is the respective covariance. If expected trace length μ_t approaches zero, the difference between equations (1) and (2) vanishes, such that σ^2_Q becomes equal to the variance σ^2_{Qa} of approximation Q_a. For a normalized transect and assuming spatially constant density and trace length parameters, the variance of trace midpoints in the transect is $A_T \lambda_{\mathrm{norm}}$, such that $\sigma^2_{Qa} = A_T \lambda_{\mathrm{norm}} \mu^2_{\tau} q^2$. Knowing from equation (13) that $\lambda_{\mathrm{norm}} \mu_\tau = 1/(N_{\mathrm{well}} \cos\vartheta) = \mathrm{constant}$ to maintain unit expectation of intersection, σ^2_{Qa} goes to zero as μ_τ goes to zero. This is valid for arbitrary values of ϑ (or θ) and may be generalized to spatial trends in λ_{norm} and μ_τ. As a consequence, $\mathrm{Cov}(Q^*,Q)$ also approaches zero, and equation (C1) reduces to $\sigma^2_e = \sigma^2_{Q^*}$. For $q_j^* = q_j = \mathrm{constant}$ and $\theta_j = \mathrm{constant}$, Q^* from equation (7) may be written as

$$Q^* = \frac{A_T q_j^*}{\cos\theta_j} \sum_{k=1}^{N_{\mathrm{well}}} \frac{N_{jk}\omega_k}{L_k}, \tag{C2}$$

where ω_k/L_k is constant for each FRPFM, and N_{jk} is the random number of intersections per FRPFM. With this

$$\sigma^2_{Q^*} = \left(\frac{A_T q_j^*}{\cos\theta_j}\right)^2 \sum_{k=1}^{2N_{\mathrm{well}}} \mu_{Njk} \left(\frac{\omega_k}{L_k}\right)^2 = \left(\frac{A_T q_j^*}{\cos\theta_j}\right)^2 \mu_{Nj} \mu'_{(\omega/L)^2}, \tag{C3}$$

where use is made of the Poisson property that the variance of N_{jk} is equal to its expectation μ_{Njk}, and $\mu'_{(\omega/L)^2}$ denotes the average of $(\omega_k/L_k)^2$ after weighting by μ_{Njk} (the prime indicating the weighting involved and remembering $\mu_{Nj} = \sum_{k=1}^{N_{\mathrm{well}}} \mu_{Njk}$). The expectation μ_{Q^*} of equation (C2) is found as

$$\mu_{Q^*} = \frac{A_T q_j^*}{\cos\theta_j} \sum_{k=1}^{N_{\mathrm{well}}} \mu_{Njk} \frac{\omega_k}{L_k} = \frac{A_T q_j^*}{\cos\theta_j} \mu_{Nj} \mu'_{\omega/L}, \tag{C4}$$

where $\mu'_{\omega/L}$ is the average of ω_k/L_k after weighting by μ_{Njk}. Using $\mu_{Nj} = 1$ (as imposed by normalization in section 3.1) in equations (C3) and (C4) results in $CV^2_{e,\mathrm{max}} = \sigma^2_{Q^*}/\mu^2_{Q^*} = \mu'_{(\omega/L)^2}/\mu'^2_{\omega/L}$ and the first expression in equation (18) (note that $\mu'_{(\omega/L)^2} = \mu'^2_{\omega/L} + \sigma'^2_{\omega/L}$). The second expression in equation (18) is obtained analogously, except for using the first expressions of equations (C3) and (C4) after division of $\sigma^2_{Q^*}$ and μ_{Q^*} by total number of intersections N_{set} (normalization to single intersection) and substituting μ_{Njk} by its unbiased estimates N_{jk}. In equation (18) we further substitute N_{PFM} and N_k for N_{set} and N_{jk}, respectively, which makes $\mathrm{CV}_{e,\mathrm{max}}$ valid for all traces (not just one set) and which implies the assumption that spatial trends in trace density or trace length are the same for all trace sets (i.e., μ_{Njk} and μ_{Nk} are proportional).

[49] **Acknowledgments.** This research was funded by the U.S. Department of Defense (project number ER0831) under the Environmental Security Technology Compliance Program (ESTCP). H.K. also gratefully acknowledges support from a fellowship of the Bahia State Science Foundation (FAPESB; DCR 0001/2009), Brazil. We are thankful to Michael Cardiff and two anonymous reviewers, who helped improving the presentation of our work.

References

Annable, M. D., K. Hatfield, J. Cho, H. Klammler, B. L. Parker, J. A. Cherry, and P. S. C. Rao (2005), Field-scale evaluation of the passive flux meter for simultaneous measurement of groundwater and contaminant fluxes, *Environ. Sci. Technol.*, *39*(18), 7194–7201.

Baecher, G. B., N. A. Lanney, and H. H. Einstein (1977), Statistical description of rock properties and sampling, in *Proceedings, 18th United States Symposium on Rock Mechanics*, Colorado School of Mines, Golden, Colorado, pp. 5C1–5C8, Johnson.

Basu, N. B., P. S. C. Rao, I. C. Poyer, M. D. Annable, and K. Hatfield (2006), Flux-based assessment at a manufacturing site contaminated with trichloroethylene, *J. Contam. Hydrol.*, *86*(1–2), 105–127.

Beland-Pelletier, C., M. Fraser, J. Barker, and T. Ptak (2011), Estimating contaminant mass discharge: A field comparison of the multilevel point measurement and the integral pumping investigation approaches and their uncertainties, *J. Contam. Hydrol.*, *122*(1–4), 63–75.

Berkowitz, B. (2002), Characterizing flow and transport in fractured geological media: A review, *Adv. Water Resour.*, *25*(8–12), 861–884.

Cai, Z., R. D. Wilson, M. A. Cardiff, and P. K. Kitanidis (2011), Increasing confidence in mass discharge estimates using geostatistical methods, *Ground Water*, *49*(2), 197–208.

Cherry, J., B. Parker, and C. Keller (2007), A new depth-discrete multilevel monitoring approach for fractured rock, *Ground Water Monit. Rem.*, *27*(2), 57–70.

Chiles, J. (2005), Stochastic modeling of natural fractured media: A review, in *Geostatistics Banff 2004*, edited by O. Leuangthong and C. Deutsch, pp. 285–294, Springer, The Netherlands.

Chiles, J.-P., and G. de Marsily (1993), Stochastic models of fracture systems and their use in flow and transport modeling, in *Flow and Contaminant Transport in Fractured Rock*, edited by J. Bear, C.-F. Tsang, and G. de Marsily, pp. 169–236, Academic, San Diego, Calif.

Cho, J., M. A. Newman, H. Klammler, K. Hatfield, M. D. Annable, B. L. Parker, J. A. Cherry, P. Pehme, R. Kroeker, and W. H. Pedler (2011), Quantifying groundwater and contaminant flux in fractured rock, in *Proceedings of the American Geophysical Union Annual Fall Meeting*, San Francisco, Calif., 5–9 Dec.

Dietrich, P., R. Helmig, M. Sauter, H. Hötzl, J. Köngeter, and G. Teutsch (Eds.) (2005), *Flow and Transport in Fractured Porous Media*, Springer, Berlin.

Faybishenko, B., P. A. Witherspoon, and S. M. Benson (Eds.) (2000), *Dynamics of Fluids in Fractured Rock*, Am. Geophys. Union, Washington, D. C.

Faybishenko, B., P. A. Witherspoon, and J. Gale (Eds.) (2005), *Dynamics of Fluids and Transport in Fractured Rock*, Am. Geophys. Union, Washington, D. C.

Feenstra, S., J. A. Cherry, and B. L. Parker (1996), Conceptual models for the behavior of DNAPLs in the subsurface, in *Dense Chlorinated Solvents and Other DNAPLs in Groundwater*, edited by J. F. Pankow and J. A. Cherry, chap. 2, Waterloo Press, Portland, Oreg.

Goovaerts, P. (1997), *Geostatistics for Natural Resources Evaluation*, Oxford Univ. Press, New York.

Hatfield, K. (2010), Demonstration and validation of a fractured rock passive flux meter, *Federal Remediation Round Table*, pp. 5–7, Washington,

D. C., 9 Nov. [Available at www.frtr.gov/pdf/meetings/nov10/FA_2010_mtg_summary.pdf.]

Hatfield, K., M. D. Annable, J. Cho, P. S. C. Rao, and H. Klammler (2004), A direct passive method for measuring water and contaminant fluxes in porous media. *J. Contam. Hydrol.*, *75*(3–4), 155–181.

Helmig, R. (1993), Theorie und Numerik der Mehrphasenströmungen in geklüftet-porösen Medien [Theory and numerical study of multiphase flow in fractured porous media], Bericht 34/1993, Inst. für Strömungsmechanik und Elektr., Rechnen im Bauwesen der Univ. Hannover, Eigenverlag, Hannover.

Interstate Technology & Regulatory Council (ITRC) (2010), *Technology Overview: Use and Measurement of Mass Flux and Mass Discharge, MASSFLUX-1*, Washington, D. C.

Kingman, J. F. C. (1993), *Poisson Processes. Oxford Studies in Probability: 3*, Clarendon Press, Oxford Univ. Press, New York.

Klammler, H. (2004), Conceptual models for advanced monitoring of subsurface and surface water and contaminant fluxes, Ph.D. dissertation, Graz Univ. of Technol., Austria.

Klammler H., K. Hatfield, M. D. Annable, E. Agyei, B. Parker, J. Cherry, and P. S. C. Rao (2007), General analytical treatment of the flow field relevant to the interpretation of passive fluxmeter measurements, *Water Resour. Res.*, *43*, W04407, doi:10.1029/2005WR004718.

Klammler, H., K. Hatfield, M. D. Annable, B. L. Parker, and J. Cherry (2008), Device and method for measuring fluid fluxes, solute fluxes and fracture parameters in fractured flow systems, Patent [US7334486], U.S. Patent.

Klammler, H., et al. (2012), Contaminant discharge and uncertainty estimates from passive flux meter measurements, *Water Resour. Res.*, *48*, W02512, doi:10.1029/2011WR010535.

Li, K. B., P. Goovaerts, and L. M. Abriola (2007), A geostatistical approach for quantification of contaminant mass discharge uncertainty using multilevel sampler measurements, *Water Resour. Res.*, *43*, W06436, doi:10.1029/2006WR005427.

Long, J. C. S., and P. A. Witherspoon (1985), The relationship of the degree of interconnection to permeability in fracture networks, *J. Geophys. Res.*, *90*(B4), 3087–3098.

Newman, M. A., K. Hatfield, H. Klammler, M. D. Annable, J. Cho, B. L. Parker, J. A. Cherry, R. Kroeker, and W. H. Pedler (2009), Demonstration and validation of a fractured rock passive flux meter, in *Proceedings: SERDP/ESTCP Partners in Environmental Technology Technical Symposium*, Washington, D. C., 30 Nov.–2 Dec.

Newman, M. A., J. Cho, K. Hatfield, H. Klammler, M. D. Annable, B. L. Parker, J. A. Cherry, R. Kroeker, and W. H. Pedler (2010), Characterizing groundwater and contaminant flux in fractured rock systems, in *Proceedings of the American Geophysical Union Annual Fall Meeting*, San Francisco, Calif, 13–17 Dec.

Nichols, E., and T. Roth (2004), Flux redux: Using mass flux to improve cleanup decisions, *L.U.S.T.Line 46* (March), N. Engl. Interstate Water Pollut. Control Comm., Lowell, Mass.

Novakowski, K., G. Bickerton, P. Lapcevic, J. Voralek, and N. Ross (2006), Measurements of groundwater velocity in discrete rock fractures, *J. Contam. Hydrol.*, *82*(1–2), 44–60.

Pehme, P., B. Parker, J. Cherry, and J. Greenhouse (2010), Improved resolution of ambient flow through fractured rock with temperature logs, *Ground Water*, *48*(2), 191–205.

Reeves, D. M., K. F. Pohlmann, G. M. Pohll, M. Ye, and J. B. Chapman (2010), Incorporation of conceptual and parametric uncertainty into radionuclide flux estimates from a fractured granite rock mass, *Stochastic Environ. Res. Risk Assess.*, *24*, 899–915.

Robertson, A. (1970), The interpretation of geological factors for use in slope stability, in *Proceedings, Symposium on the Theoretical Background to the Planning of Open Pit Mines With Special Reference to Slope Stability*, pp. 55–71, S. Afr. Inst. of Min. and Metal., Johannesburg, S. Afr.

Schwede, R. L., and O. A. Cirpka (2010), Stochastic evaluation of mass discharge from pointlike concentration measurements, *J. Contam. Hydrol.*, *111*(1–4), 36–47.

Troldborg, M., W. Nowak, N. Tuxen, P. L. Bjerg, R. Helmig, and P. J. Binning (2010), Uncertainty evaluation of mass discharge estimates from a contaminated site using a fully Bayesian framework, *Water Resour. Res.*, *46*, W12552, doi:10.1029/2010WR009227.

Verreydt, G., J. Bronders, I. Van Keer, L. Diels, and P. Vanderauwera (2010), Passive samplers for monitoring VOCs in groundwater and the prospects related to mass flux measurements, *Ground Water Monit. Rem.*, *30*(2), 114–126.